Journal of Molecular Structure 1229 (2021) 129799

Contents lists available at ScienceDirect

Journal of Molecular Structure

journal homepage: www.elsevier.com/locate/molstr

Experimental and first-principles study of a new hydrazine derivative for DSSC applications

Ismail Badran[a,*], Said Tighadouini[b], Smaail Radi[c], Abdelkader Zarrouk[d], Ismail Warad[a,*]

[a] Department of Chemistry and Earth Sciences, PO Box 2713, Qatar University, Doha, Qatar
[b] Laboratory of Organic Synthesis, Extraction and Valorization, Faculty of Sciences Ain Chock, Hassan II University, Route d'El Jadida Km 2, BP: 5366, Casablanca, Morocco
[c] Laboratory of Applied and Environmental Chemistry (LCAE), Mohammed First University, Oujda, Morocco
[d] Laboratory of Materials, Nanotechnology and Environment, Faculty of Sciences, Mohammed V University, Av. I bn Battouta, Box 1014, Agdal-Rabat, Morocco

ARTICLE INFO

Article history:
Received 3 November 2020
Revised 13 December 2020
Accepted 16 December 2020
Available online 21 December 2020

Keywords:
hydrazine
DFT
TDDFT
exo-endo isomerization
DSSC
dye-sensitized
optical activity

ABSTRACT

Hydrazine derivatives have a wide variety of applications in organic synthesis, material science, medical treatments, as well as the dye-sensitized solar cells (DSSC). In this work, the molecular structure, electronic spectra and first principles investigation for the *exo-endo* isomerization in (1E,2E)-bis[1-(4-nitrophenyl)ethylidene]hydrazine were studied. The structural interactions and synthon formations have been determined experimentally via Hirshfeld surface analysis (HSA) and two-dimensional fingerprint plots (2D-FP). Furthermore, the solid-state XRD/HSA interactions have been used to explain the physical behavior of the compound. The transition state for the *exo-endo* isomerization was located using density functional theory (DFT). The activation barrier is estimated to be 110.5 kJ/mol (in *vacuo*). The *endo* isomer was found to be slightly more stable than the *exo* one. The UV-Vis spectra of the two isomers were obtained using time-dependent density functional theory (TDDFT) and compared to the experimental spectra in *vacuo*, water, and methanol. To explore the potential of the new compound as a DSSC sensitizer, the emission spectrum was also constructed by optimizing the *singlet* electronic excited state.

Introduction

Hydrazine derivatives are a group of organic compounds containing a C=N–N=C functional group. Such π-conjugated system allows electronic excitations in the visible and near-UV region. This is of a special interest for many applications such as dye-sensitized solar cells (DSSC) [1–4], fluorescent probes for analytical detection [5], corrosion inhibition [6,7], and organogels [8]. In addition, phenyl substituted hydrazines were proved to exhibit antioxidant, antibacterial, and antitumor activities [9] [10].

DSSC are a new generation of power devices that incorporate an organic dye grafted on a semiconductor surface with a wide bandgap, such as TiO_2 or ZnO [1,3,4,11]. DSSC can be considered good alternatives for the conversional silicon-based solar cells due to their low cost and weight, easy fabrication, and their ability to function under low-light (cloudy) conditions [4,11–13]. However, recent advancements of DSSC have not succeeded in fabricating devices with efficiencies greater than 12%. Also, employing a liquid dye that could evaporate at high temperatures is another drawback of DSSC. Therefore, there is increasing interest in developing solid-state DSSC, where solid hydrazine derivatives can come into play as potential photosensitizers [14–16].

The acting principle behind DSSC requires an organic compound with a donor-acceptor structure which allows electron density movement within the molecule moiety [1,12]. This *push-pull* mechanism initiates the DSSC reaction by an excitation of the sensitizer, typically from the highest occupied molecular orbital (HOMO) to the lowest unoccupied molecular orbital (LUMO), followed by an electron transfer into the conduction band of the semiconductor [4,11,12,16]. For a successful DSSC device, the organic sensitizer should [11,16]:

1. be thermally and chemically stable with hydrophobic groups to enhance the long-term stability of DSSC.
2. absorb in the visible and near ultraviolet regions of the electromagnetic spectrum to allow maximum sunlight harvesting.
3. have a HOMO-LUMO difference that is slightly higher than the conduction band of the operating semiconductor.

* Corresponding authors.
E-mail addresses: ibadran@qu.edu.qa (I. Badran), ismail.warad@qu.edu.qa (I. Warad).

https://doi.org/10.1016/j.molstruc.2020.129799

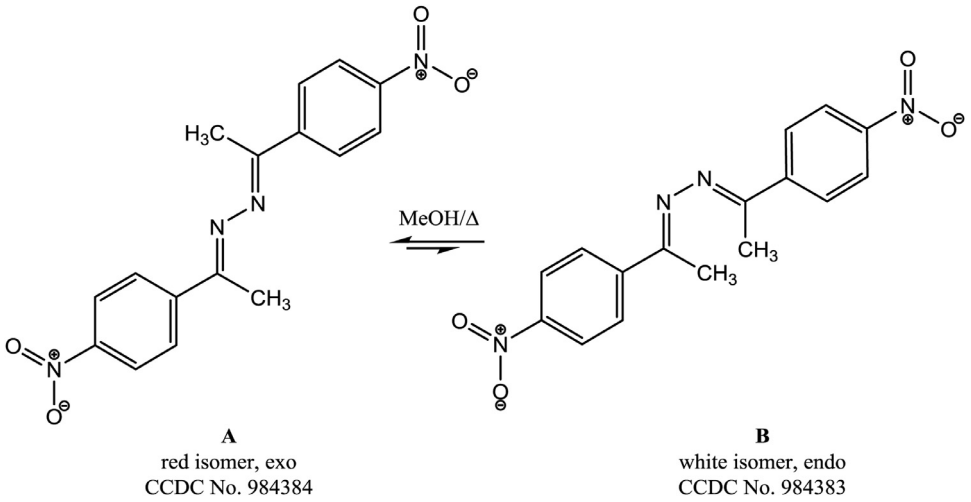

Scheme 1. *exo-endo* isomerization in (1E,2E)-bis[1-(4-nitrophenyl)ethylidene]hydrazine.

In our recent work, the compound, (1E,2E)-bis[1-(4-nitrophenyl)ethylidene]hydrazine (CCDC No. 984384 and 984383), was synthesized from hydrazine hydrate and 4-nitroacetophenone solutions [17,18]. The compound was recrystallized in methanol and its structure was verified using single-crystal XRD. A mixture of white and red crystals was isolated at room temperature. Upon heating in methanol, the red isomer was completely converted into the white one. As revealed by the XRD analysis, this conversion was attributed to an *exo/endo* isomerization as shown in Scheme 1. This type of geometrical isomerization, which can also described as a *cis-trans* one, is important for DSSC action due to the twisted intramolecular charge transfer (TICT) process [19,20].

The motivation of this study was to comprehend the isomerization in this compound, and to shed more light into its electronic behavior. Detailed structural and Hirshfeld surface analysis based on the XRD data was done to reveal the intermolecular interactions within the crystal structure. Also, a search for the transition state, using first-principle methods, that connect the two isomers was done. The thermochemical quantities ΔH, ΔG, and ΔS for both the activation step and the whole reaction were computed. As revealed from the calculations of this work. The widely used B3LYP density functional was unable to describe the molecular geometries of both the *exo* and *endo* isomers. Despite its success in a massive number of studies, the performance of the B3LYP functional is recently under question [21–23]. Thus, different group of hybrid, mixed, and standalone DFT functionals were tested in this work, this includes BHandH, B3PW91, TPSSh, APFD, MN15, and MN12L.

In addition to the ground state calculations, a TDDFT calculations were employed to probe the excited states of the two isomers. The UV-Vis spectra obtained from these calculations were compared to the experimental ones. Also, the molecular orbitals involved in the excitations were mapped in order to comprehend the electronic transitions in the hydrazine compound, which are important to its application as a DSSC photosensitizer.

According to Labat *et al.*, one must use the same level of theory in treating all ground and excited states involved in any *ab-intio* calculations related to DSSC [3]. Therefore, extra care was taken to address this point in this work. In addition, the 2nd order Møller–Plesset perturbation theory (MP2) [24,25] was implemented to compute the final single point energies of all species in order to ensure accurate results.

Experimental section

Materials and XRD analysis

(1E,2E)-bis[1-(4-nitrophenyl)ethylidene]hydrazine was synthesized as described in our recent work [17], and can be fouind in the Cambridge Crystallography data base, CCDC No. 984384 and 984383 [18]. The structural and Hirshfeld surface analysis (HSA) was done using Crystal Explorer 3.1 [26], and Mercury 3.0 [27].

Thermogravimetric analysis (TGA)

The TGA analysis was done using an SDT-Q600 thermal analyzer (TA instrument, New Castle, Delaware, USA). The mass loss of the title compound was recorded as a function of temperature in air between 25°C and 800°C at a heating rate of 5°C/min. A constant air flow of 30 cm^3 min^{-1} was maintained during the experiment.

Absorption spectra

The absorption spectra were recorded in methanol at room temperature using a Pharmacia LKB-Biochrom 4060 spectrophotometer. Two-sided quartz cuvettes were used in order to cover both the UV and visible ranges.

Theoretical calculations

Initial guesses for the *exo* and *endo* isomers were taken from the XRD data and used to optimize the molecules in the gas phase using different DFT functionals and the 6-31+G(d,p) basis set. The functionals include, B3LYP [28], BHandH [29], B3PW91 [30], TPSSh [31], APFD [32], MN15 [33], and MN12L [34]. A frequency calculation was requested with every optimization in order to ensure no imaginary frequencies exist. The transition state (TS) for the *exo-endo* isomerization was located and verified to have a single imaginary frequency. To ensure the authenticity of the TS, an intrinsic reaction coordinates (IRC) calculation was requested and the *exo* and *endo* isomers were verified to branch out the TS.

In order to obtain meaningful results, the 2nd order Møller–Plesset perturbation theory (MP2) [24,25] was implemented using the 6-311+G(d,p) basis set to compute the single point energies for all species involved in this work. This method was proven to show good results for similar systems [35–39]. Zero-point energies (ZPE)

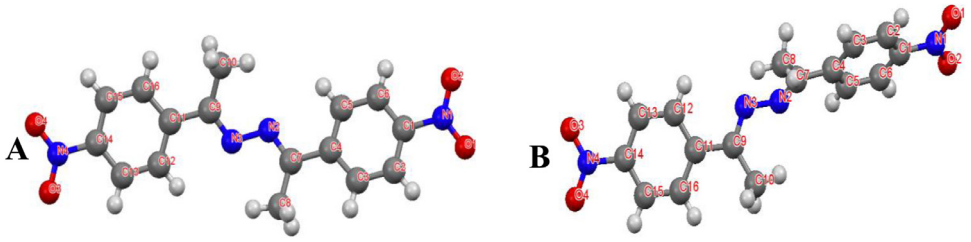

Fig. 1. Molecular structures of A isomer (*exo*) and B isomer (*endo*), obtained from XRD data [17].

were used without any scaling, and *singlet* ground state was assumed for all closed shell species unless mentioned otherwise. The TDDFT calculations were done using the same level of theory. Solvation calculations were done via the polarizable continuum model (PCM) [40,41], by using the SCRF=solvent keyword in Gaussian. Further description of the computational calculations involved in this work were reported in previous publications [37,42,43,57]. All calculations were done using Gaussian 16 Rev C.01 [44] and viewed using Gaussview [45].

Results and discussion

The exo-endo *solid-state interactions*

The experimental molecular structures for the two isomers, A (*exo*) and B (*endo*), were obtained from the single-crystal XRD data [17] and are illustrated in Fig. 1. Crystal structures of solids can be depicted as three-dimensional networks with molecules conceded as nodes and intermolecular interactions as connections [46,47]. Describing the supramolecular synthons within the crystal structure has a unique significance in retro organic syntheses as well as understanding the packing within the crystal [47].

Our crystal analysis revealed that the two isomers exhibit different interaction patterns. A strong hydrogen bond interaction was observed between the phenolic hydrogen and the terminal nitro group ($C_{Ph/Me}$-H…..ONO). Interestingly, no C-H●●●N hydroge bonds were observed, Other weaker interactions such as π-π stacking were found in both isomers and a C-H...π was found only within the **A** isomer lattice. Three types of supramolecular synthons of the type $R^2_2(26)$, $R^2_2(24)$, and $R^2_2(7)$ have been detected in the packing diagrams as shown in Fig. 2. In the **A** isomer, a supramolecular synthon $R^2_2(24)$ was connected *via* two similar C_{Me}-H….ONO at a close distance of 2.660 Å (Fig. 2a). Two similar synthons were detected in the B isomer: one with two 2.642 Å C_{Me}-H….ONO H-bonds and two π-π rings stacking with 3.543 Å lengths (Fig. 2e), and the second was with C_{Ph}-H….ONO at a distance of 2.442 Å and π_{ring} - π_{ring} stacking with 3.334 Å (Fig. 2f). A unique $\pi_{(N=C)}$-π_{ring} with 3.331 Å and C_{Me}-H...π_{ring} at a distance of 2.784 Å were detected in isomer A only (Fig. 2b). Moreover a $R^2_2(26)$ supramolecular synthon was established *via* two of C_{Me}-H….ONO- with 2.507 Å only in isomer **B** (Fig. 1g). Two novel $R^2_2(7)$ [H…ONO….H] at 2.408 and 2.642 Å were also detected (Fig. 2c). However, novel $R^2_2(24)$ synthon via two of C_{Me}-H….ONO- with 2.604 Å including two ONO…. π_{ring} with 3.190 distances (Fig. 2h). The two compounds agreed to create two 1D classical C_{Me}-H….ONO at 2.660 Å and C_{Ph}-H….ONO at 2.672 Å (Fig. 1d) and 1D of two C_{Ph}-H….ONO at 2.528 and 2.640 Å in **B** (Fig. 2i).

Since hydrogen bonds interactions are considered to be the strongest among other intermolecular forces, their presence reflects the rigidity and of the compound. Because isomer **B** exhibit 10 types of C-H….ONO hydrogen bonds, while isomer **A** has only 6 types. Isomer **B** is considered more rigid than **A**. This observation has some interesting consequences on the physical and optical properties of the two isomers, as shown in the following pages.

Table 1
Structural parameters of **A** (*exo*) and B (*endo*). experimental values were obtained from ref. [17]. Theoretical values were obtained at MP2/6-311+G(d,p)//APFD/6-31+G(d) level of theory.

Species	R1 (Me-Me) (Å)	D1 (C7-N2-N3-C9) (°)	A1 (Me-N2-Me) (°)
B (*endo*) (exp.)	**4.11**	**66.6**	**103.0**
B (*endo*) (calc.) in *vacuo*	4.47	50.7	117.8
B (*endo*) (calc.) in *water*	4.22	62.9	107.5
B (*endo*) (calc.) in *methanol*	4.24	62.2	106.1
A (*exo*), exp.	**4.82**	**155.2**	**138.2**
A (*exo*), (calc.) in *vacuo*	4.81	150.8	134.8
A (*exo*), (calc.) in *water*	4.67	140.8	126.6
A (*exo*), (calc.) in *methanol*	4.68	141.3	127.2
TS (calc.) in *vacuo*	4.65	1.2	124.0
TS (calc.) in *water*	4.62	0.6	123.2
TS (calc.) in *methanol*	4.62	0.7	123.3

Hirshfeld analysis

Surface properties and molecular interactions of both crystals structures were obtained via HSA and two-dimensional fingerprint plots (2D-FP), which were performed by Crystal Explorer. The XRD data were used to construct the geometries and the HSA intermolecular interactions, as illustrated in Fig. 3. The HSA analysis allows the visualization of interactions between molecules through color coding of the surface. The normalized contact distance (d_{norm}) is a parameter that measures the Van der Waals' short and long interactions [48–50]. As shown in Fig. 3, the d_{norm} of the HSA mapped on the surface of **B** isomer shows the presence of 14 red large spots, compared to 10 red spots of isomer **A**. In both isomers, the strongest interactions are H-bonds due to C-H….O-NO interactions are indicated by large red holes. Interestingly, no H….N H-bonds were detected in lattices of both isomers, in agreement with the synthon structure shown earlier. Furthermore, the 2D-FP maps of the sum of the interactions participating to the HSA surface are illustrated in Fig. 4. It was determined that the intermolecular interactions follow the trend: H….H > H….O > H…C > H….N, in both isomers. Overall, the HSA and the 2D-FP analysis are in concert with the results obtained from the XRD analysis.

Theoretical study of the exo-endo *isomerization*

For the sake of this discussion, the following structural parameters are defined from the structures of Fig. 1: R1 is the C8-C10 (methyl-methyl) bond distance. A1 is the C8-N3-C10 bond angel. D1 is the C7-N2-N3-C9 dihedral angle. Table 1 lists the experimental parameters for both isomers. The *exo* isomer has a planar structure with D1= 155.2°, while the *endo* isomer has a D1 value of 66.6°. The difference between the two also lies in the value of R1, the methyl-methyl distance, which is 4.82 and 4.11 Å, respectively.

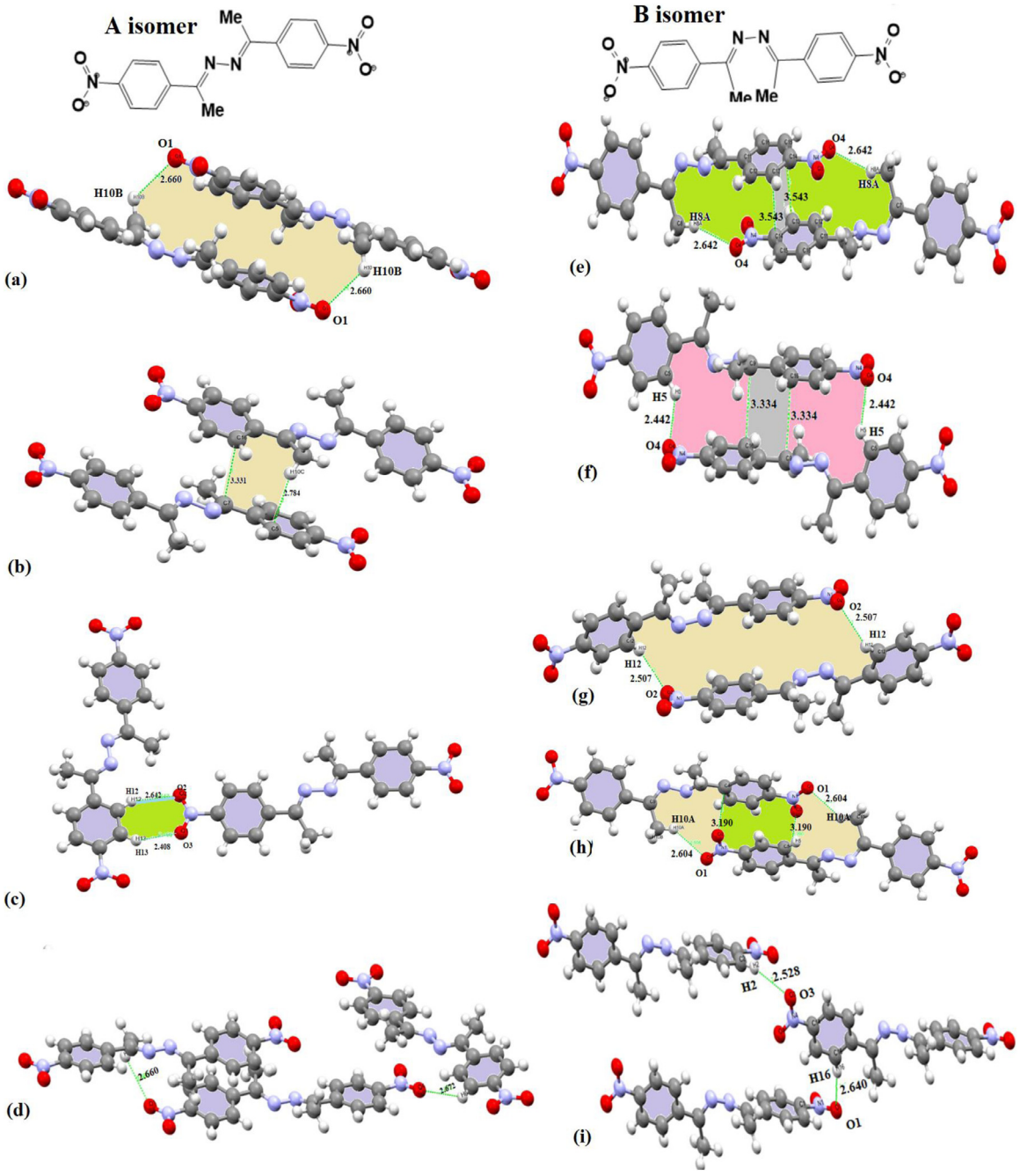

Fig. 2. Total molecular interactions within the crystal lattice of the **A** and **B** isomers.

When this compound was first prepared [17], a mixture of the two isomers was obtained at room temperature. Upon heating in methanol, the **A** (*exo*) isomer was converted into the **B** (*endo*) as explained in the introduction (*cf.* Scheme 1). In order to understand this behavior, we attempted to optimize the two structures using the widely used B3LYP functional with a variety of basis sets and initial molecular guesses. All the optimizations have converged into a semi-structure that lies between the two isomers with a D1 value of 138° and R1 = 4.64 Å. Thus, we attempted to optimize the two isomers again using different DFT functionals as mentioned in the theoretical section. Both the APFD and MN12L functionals were able to locate closer geometries to the experimental structures. The Austin-Frisch-Petersson (APFD) is a hybrid functional that was proposed in 2012 and does include corrections for dispersion [32]. The MN12L, on the other hand, is a standalone pure functional that was proposed by Peverati and Truhlar [34]. In this study, the results from APFD calculations were adapted because they showed the best agreement with the experimental values. Fig. 5 shows the optimized structures (in *vacuo*) for **A**, and **B**, along with the isomerization transition state that was located at the same level of theory (MP2/6-311+G(d,p)//APFD /6-31+G(d)). In addition to the gas-phase calculations, further optimizations were done in water and methanol in order to study their effect on the structure. The parameters, R1, D1, and A1 for all the species are tabulated in Table 1. By considering the theoretical calculations done in the gas phase, the results demonstrate good agreement with the experimental parameters. The percent errors associated with the theoretical calculations based on the XRD geometries are provided in Fig. S1 (supplementary information section)

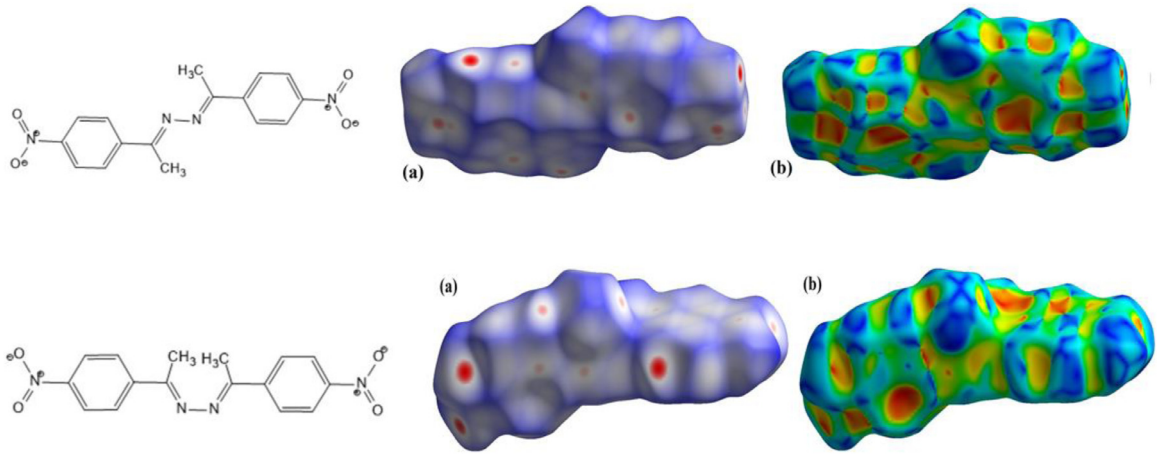

Fig. 3. Views of the Hirshfeld surfaces for isomers, **A** and **B**.

Table 2
Relative energy values, in kJ/mol for *exo-endo* isomerization in the hydrazine derivative, obtained at MP2/6-311+G(d,p)//APFD /6-31+G(d) level of theory.

	Species	ΔH_{298}	ΔG_{298}	$T\Delta S_{298}$
In *vacuo*	**A** (*exo*)	0.0	0.0	0.0
	transition state	109.7	110.5	-0.8
	B (*endo*)	-4.1	-5.9	1.8
In *water*	**A (*exo*)**	0.0	0.0	0.0
	transition state	106.6	107.8	-1.2
	B (*endo*)	-5.4	-9.1	3.7
In *methanol*	**A (*exo*)**	0.0	0.0	0.0
	transition state	106.6	108.0	-1.4
	B (*endo*)	-5.3	-8.7	3.4

The transition state for the *exo-endo* isomerization was located at the APFD /6-31+G(d) level of theory. An optimized structure for the TS is shown in Fig. 5, with the structural parameters tabulated in Table 1. The TS geometry involves a planar dihedral angle (1.2°), but it has an obtuse A1 (Me-N2-Me) bond angle of 124.0°. The imaginary frequency of the TS was computed at -315.2*i* cm^{-1} and it corresponds to an N-N bond twisting, as expected for the *exo-endo* isomerization. The final energy of the TS was computed at the MP2/6-311+G(d,p) level, and the corresponding activation energy was estimated to be 110.5 kJ/mol (in *vacuo*). Fig. 6 depicts the potential energy diagram for the isomerization in *vacuo* and methanol. The relative energies for the isomerization reaction are also tabulated in Table 2. The energy barrier, in terms of Gibbs free energy at room temperature ($\Delta G^{\ddagger}_{298}$), for this process is slightly lower in methanol (108.0 kJ/mol) than that in *vacuo* (110.5). The *endo* isomer is also slightly more stable by having a negative reaction energy ($\Delta G°_{298}$) than the *exo* isomer. The $\Delta G°_{298}$ values are -5.9 and -9.1, and -8.7 kJ/mol for the gas phase, water, and MeOH, respectively. The fact that *endo* isomer has a lower free Gibbs energy that the *exo* isomer is in agreement with the results obtained in the XRD analysis (*cf.* section 3.1), where the *endo* isomer was shown to exhibit stronger hydrogen bonds holding its lattice together.

The relatively low barrier ($\Delta G^{\ddagger}_{298}$) and the exergonic values of $\Delta G°_{298}$ calculated in this work can also explain the isomerization of the red isomer (**A**) to the white isomer (**B**) that observed experimentally [17]. On another note, the entropic term ($T\Delta S_{298}$) is also listed in Table 2. The results show that the entropy increases slightly upon the transformation from the *exo* to the *endo* isomer at room temperature, and the increase become more significant when the solvent is added. This is due to the open configuration of the **B** structure which because it occupy more space than the *exo* isomer, as shown in Fig. 5. This increase in the reaction entropy can contribute to the spontaneity of the reaction, especially at high temperatures.

The absorption spectra

As mentioned in the in introduction, studying the electronic spectra of hydrazine derivatives is important to understand their potential role as dye sensitizer in DSSC. The theoretical UV-Vis spectra of the two isomers, **A** and **B**, were constructed by TDDFT calculations at the same level of theory used to optimize the ground state. In order to better describe the spectra; up to 24 excited states were explored in the calculations. Fig. 7 depicts the UV-Vis experimental (shaded orange) and the calculated (solid lines) spectra for the two isomers. The *exo* and *endo* isomers exhibit maximum experimental visible absorptions at 490 and 345 nm, respectively. The calculated λ_{max} values are close to the experimental ones. The small differences between the experimental and calculated spectra are mostly originated from optimization errors as discussed previously (*cf.* Fig. S1). As shown in Fig. 7, the calculated spectra show a hypsochromic (blue) shift when methanol is used. This led to a better agreement between the calculated spectra in methanol with the *exo* isomer. Notably, there are strong agreements between the experimental and calculated spectra in the UV region, where excitations are caused by electronic transitions to higher states at shorter wavelengths.

The visible spectra of the compound can be attributed to a π-π^* delocalized electronic excitations within the molecule [13,51]. A *push-pull* mechanism, usually called an intermolecular charge transfer (ICT), is favored to take place in the visible and near UV regions for a potential DSSC sensitizer. In order to illustrate the origin of these excitations, Table 3 lists the major UV-Vis excitations in the two isomers as obtained from the TDDFT calculations. The table shows the molecular orbitals participating in each transition along with the excitation wavelength and the oscillator strength. Most of the excitations are taking place from the HOMO to the LUMO of the molecule, or adjacent MO's; HOMO-1 and LUMO+1. Electron density plots of these orbitals are shown in Fig. 8. The HUMO and HOMO-1 are mainly distributed over the π-conjugated system, *i.e.,* the hydrazine group and benzene rings. The LUMO on the other hand, shows a π^* distribution over the conjugated system and the peripheral nitro groups. Thus, the *endo* isomer takes the strong transitions at $\lambda = 358.7$ and 337.6 nm by exciting the π electrons from the center of the molecule to the empty π^* of the nitro groups. As for the *exo* isomer, the HOMO-LUMO transition

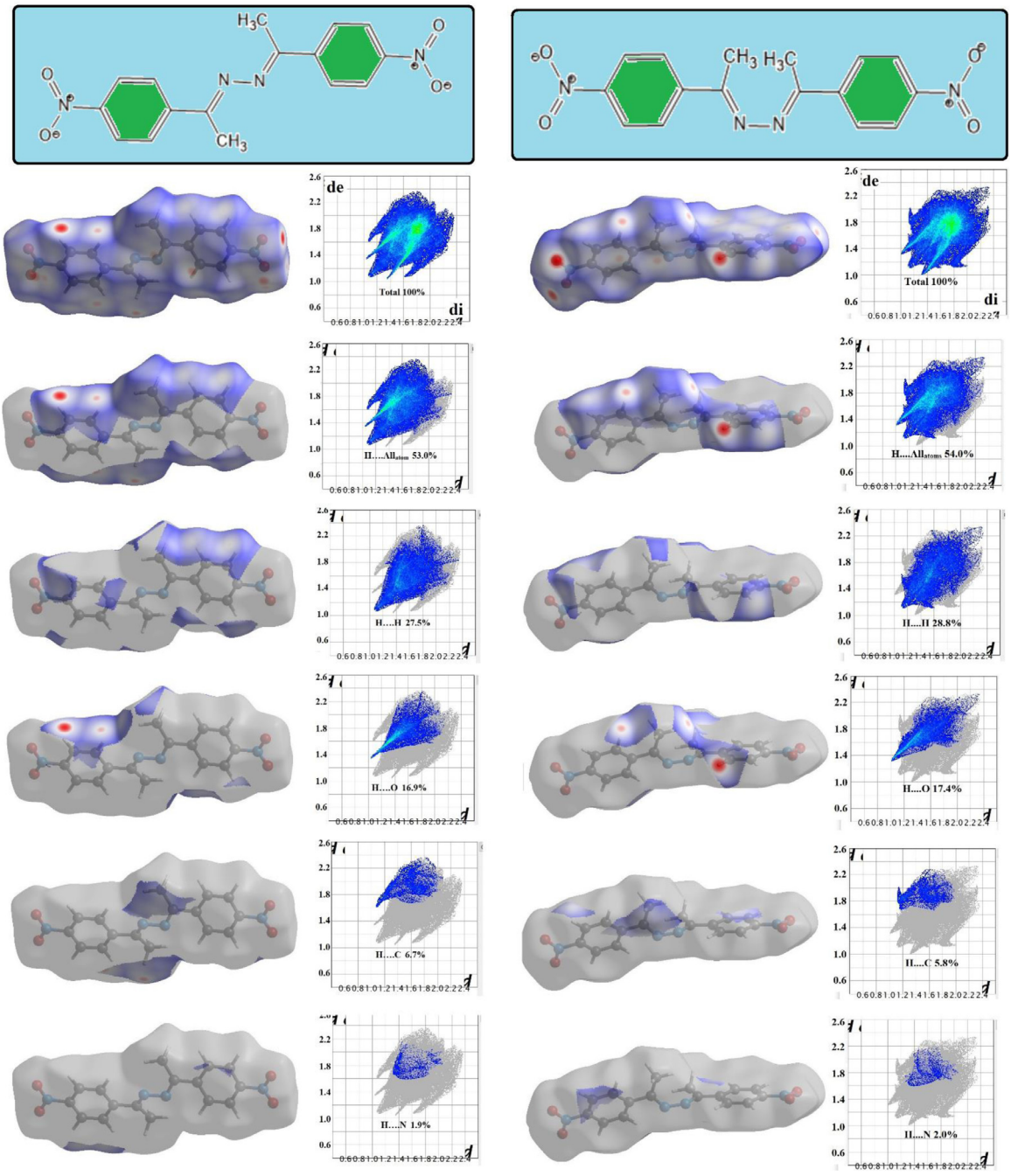

Fig. 4. 2D-FP for both isomers, **A** and **B**.

takes place at a longer wavelength, $\lambda = 407.9$. This is mostly due to the planar structure that allows faster $\pi \rightarrow \pi^*$ transitions. The *exo* isomer also undergoes a strong transition caused by a HOMO-1 $\rightarrow$ LUMO+1 at a shorter wavelength (383.2 nm). As shown in Fig. 8, the π electronic distribution in the HOMO-1 is more concentrated in the center of the molecule, while the LUMO+1 has an almost empty distribution in the center and is more concentrated on the peripherals. Thus, a $\pi \rightarrow \pi^*$ excitation will be harder in this case, causing the excitation to take place at a shorter wavelength.

Recall that the experimental λ_{max} values were observed at 490 and 345 nm, for the *exo* and *endo* isomers, respectively. The above discussion shows that these absorptions correspond mostly to a HOMO-LUMO transitions, which can be translated into the energy band gap (E_g) of the compound. These values are equivalent to 2.53 and 3.59 eV, for **A** and **B** respectively. Using the Tauc relation [52],Fig. 9, shows that the E_g values for the two isomers were calculated to be 3.11 eV for **A** and 3.37 eV for **B**, in good agreement with the experimental data.

The emission spectra

In the previous section, we illustrated that the UV-Vis spectra of the two isomers are mainly caused by a $\pi \rightarrow \pi^*$ excitation from the HOMO to the LUMO (or adjacent) orbitals. Aromatic molecules can experience fluorescence behavior that has its applications [53,54] Fluorescence occurs by an emission of a photon from an excited

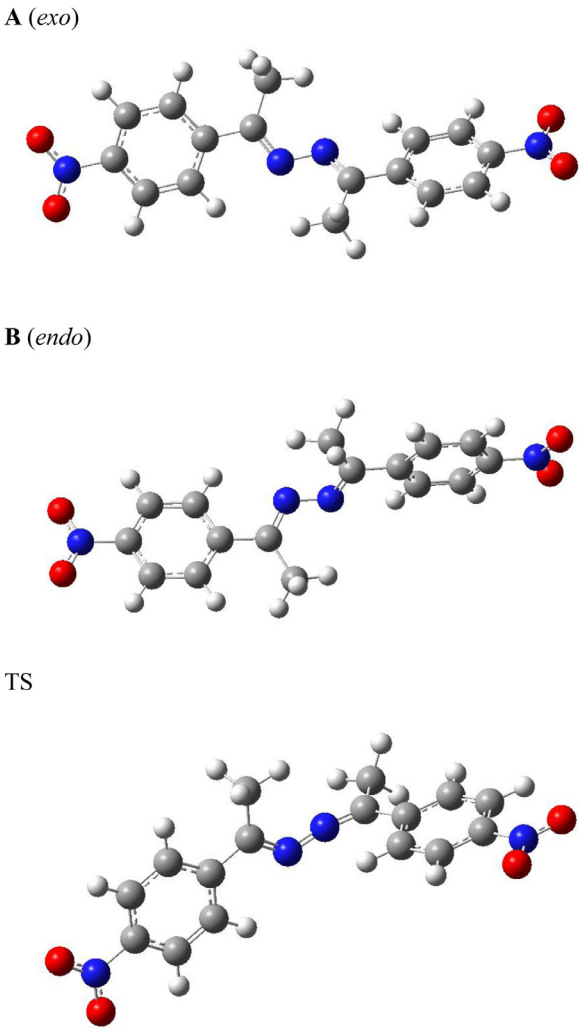

Fig. 5. Optimized structures (in *vacuo*) of A (*exo*), B (*endo*), and the isomerization transition state (TS, obtained at MP2/6-311+G(d,p)//APFD /6-31+G(d) level of theory.

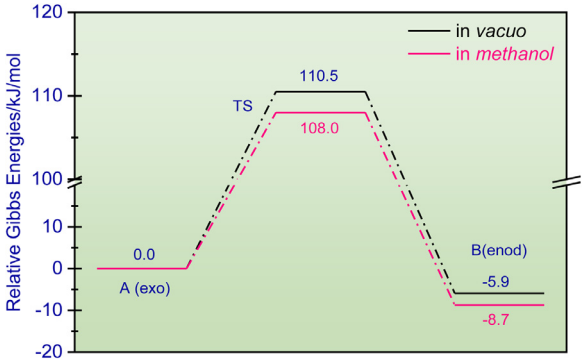

Fig. 6. Potential energy level diagram for *exo-endo* isomerization in the hydrazine derivative. Energies represent relative Gibbs free energies in kJ/mol at 298 K and 1 atm. (ZPE corrections are included).

Table 3
Types and origins of electronic excitations performed at APFD/6-31+G(d) level of theory.

	Species	Molecular orbital	λ (nm)	Oscillator strengths (f)
B (*endo*)	84 -> 86	HOMO-1 → LUMO	358.7	0.5408
	85 -> 87	HOMO → LUMO		
	84 -> 86	HOMO-1 → LUMO	337.6	0.6275
	85 -> 87	HOMO → LUMO		
	Multiple excitations	Multiple excitations	210-290 nm	0.1108
A (*exo*)	84 -> 87	HOMO-1 → LUMO+1	407.9	0.5329
	85 -> 86	HOMO → LUMO		
	84 -> 87	HOMO-1 → LUMO+1	383.2	0.4811
	85 -> 86	HOMO → LUMO		
	Multiple excitations	Multiple excitations	230-320 nm	0.1108

to the ground state with the same spin multiplicity (singlet). The emission rate is typically very fast within a timeframe of 10^{-8} s [53,54]. To explore the emission spectra for the hydrazine derivative of this work, the excited state was optimized followed by frequency and TDDFT calculations. A single excited state was located, and its structure is shown in Fig. 10. Amazingly, the excited state has a planar geometry with D1 = 0.0°. The methyl-methyl distance R1 = 5.23 Å and the angle A1 = 155.2°. The vertical excitation between the excited state and the *exo* isomer is estimated at 1.86 eV (179.5 kJ/mol) at MP2/6-311+G(d,p)//APFD /6-31+G(d) level of theory. This in good agreement with the requirements for a DSSC photosensitizer [11,16]. The emission spectrum of the excited state is compared to the excitation spectra of the two isomers, in *vacuo*, in Fig. 11. As shown, possible excitations in the UV region, at 245 and 260 nm, or the near UV, 345 and 395 nm, would lead

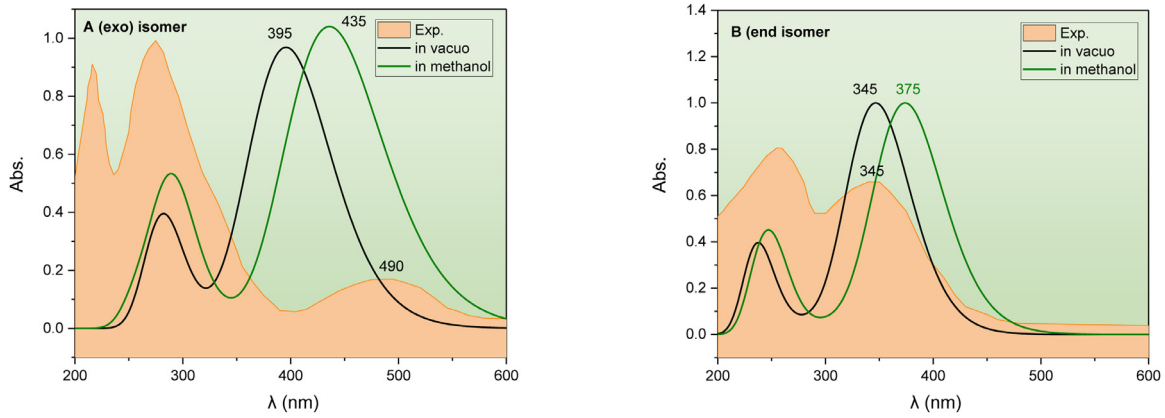

Fig. 7. Experimental (shaded orange) and calculated (solid lines) UV-Vis spectra of the two isomers, **A** and **B**. Theoretical plots were obtained at APFD /6-31+G(d) level of theory.

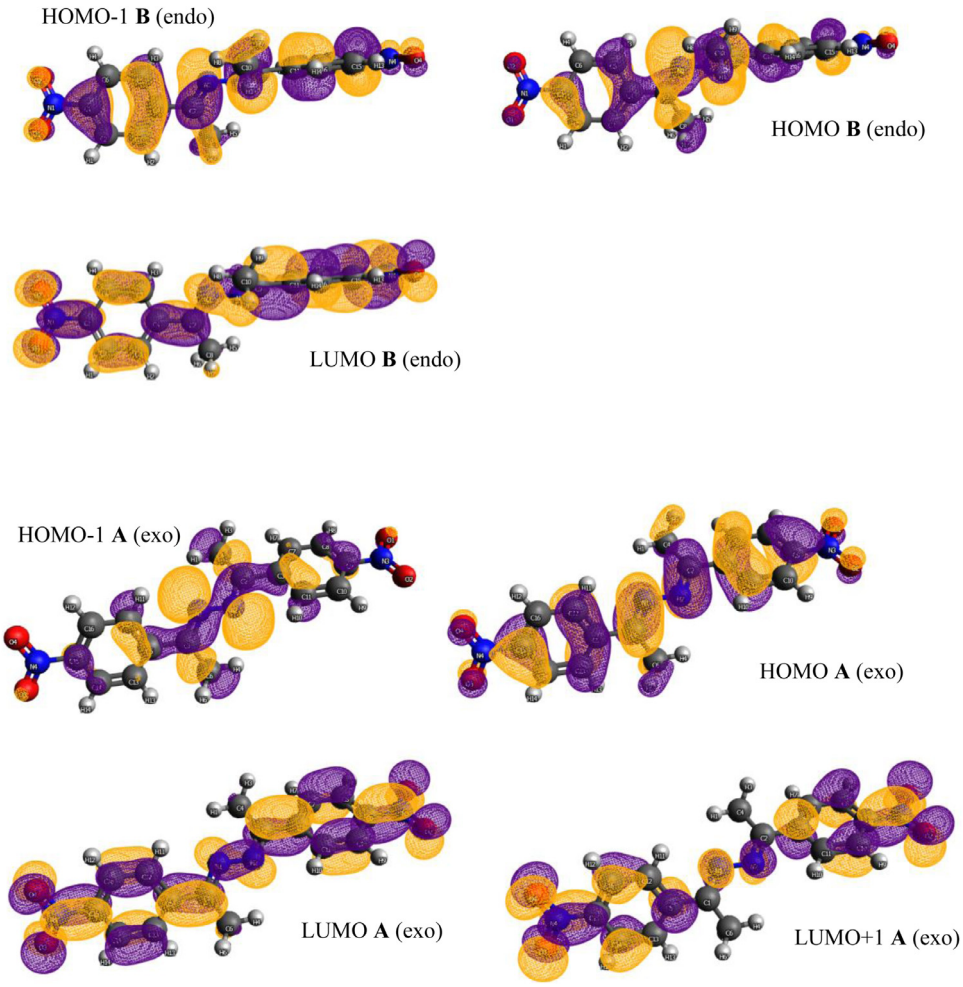

Fig. 8. Molecular orbitals participating in the major electronic excitations in the *exo* (**A**) and *endo* (**B**) isomers, obtained at APFD /6-31+G(d) level of theory.

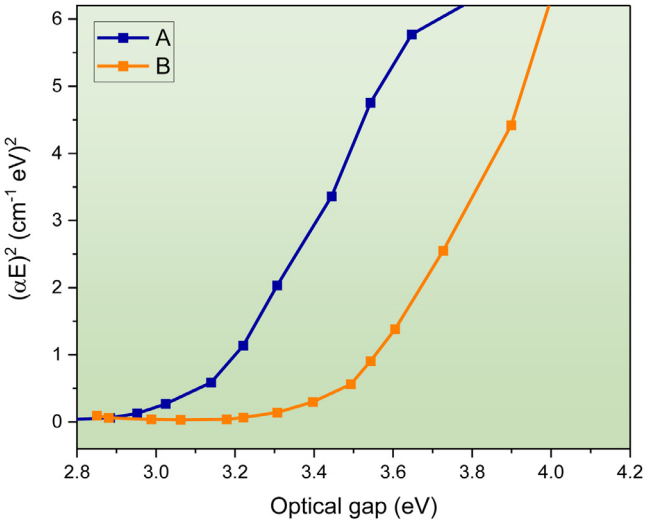

Fig. 9. Optical band gap energy in MeOH.

to an emission spectrum at 430 nm (2.88 eV). This indicates that this hydrazine derivative exhibits a fluorescent behavior and can be utilized in many applications, indulging fluorescence probes, DSSC, and biomedical sensors.

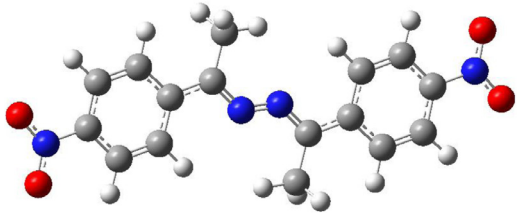

Fig. 10. Optimized structures (in *vacuo*) of the excited state. Obtained at MP2/6-311+G(d,p)//APFD /6-31+G(d) level of theory.

TG/DTG analysis

The thermal degradation of the two isomers was studied in the range of 25–900°C. The TGA and DTG curves of **A** and **B** are shown in Fig. 12. A high degree of thermal stability for both isomer has been recorded compared to the classical Schiff bases [55,56]. Both isomers decomposed completely in a single simple step mechanism with zero residue. The starting decomposition temperature (T_d) for the isomer **A** was 330°C, and 385°C for the **B** isomer, reflecting a high stability for the latter. This can be explained by the strong intermolecular forces holding the crystal structure. In section 3.1, we illustrated that isomer **B** exhibits several short H-bond interactions of the type C-H….ONO. In addition, due to the geometry of the **B** isomer (*cf.* Fig. 1 and Fig. 5), the packing in **B** is stronger than that of **A**, resulting in stringer thermal stability.

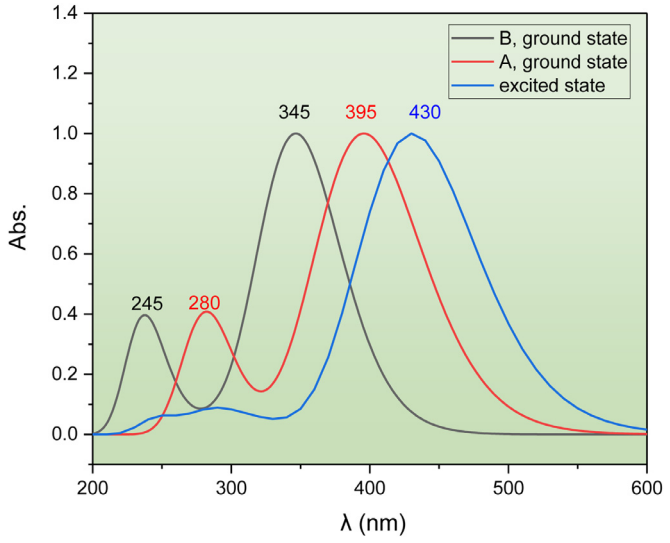

Fig. 11. Excitation spectra of the two isomers along with the emission spectra of the excited state in vacuo. Obtained at APFD /6-31+G(d) level of theory.

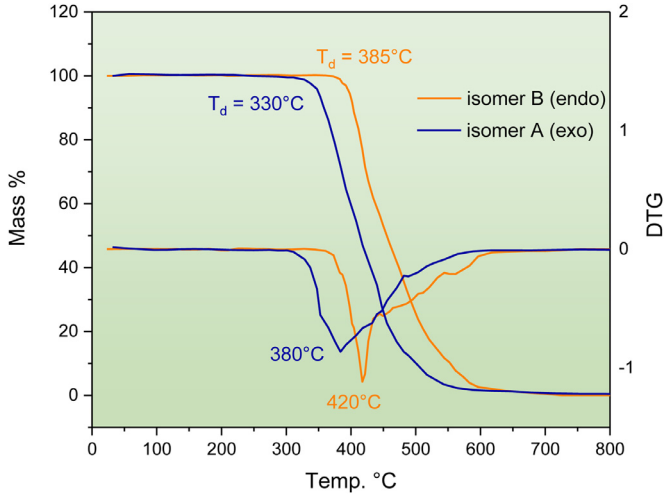

Fig. 12. TGA/DTG for A and B isomers under open atmosphere and with heating rate of 5°C min^{-1}.

Conclusions

In this work, the structure, intermolecular interactions, and electronic properties of the new hydrazine derivative were investigated for its potential use in optical applications. The crystal structural analysis revealed the formation of several synthons interactions within both the **A** (*exo*) and **B** (*endo*) structural lattice. The strongest interactions were expressed as hydrogen bonds between the phenolic protons and the terminal NO_2 groups. The **B** isomer exhibited stronger H-bonds than that of **A**, which resulted in a more rigid structure with higher stability. This has been verified by the HAS analysis. Experimentally, the **B** isomer can be easily isolated from the **A** isomer in methanol.

A theoretical study revealed that such isomerization proceeds through a transition state with a low activation barrier of 110.5 kJ/mol (in *vacuo*). The barrier is even lower in methanol and water. In addition, the **B** (*endo*) isomer was shown to be more stable than the A (*exo*) isomer by *ca.* 6 kJ/mol, in agreement with XRD analysis. The absorption spectra of the compound were studied using TD-DFT and correlated to the experimental ones. It was determined that the maximum absorption lies in the visible region and it corresponds to a π-π^* delocalized electronic transition within the molecule. The electronic excitations behind this transition were attributed to a HOMO-LUMO and adjacent orbitals. Through optimizing the excited state of the molecule, the emission spectrum was probed, and the vertical energy gap determined to be 2.88 eV. Finally, the TGA analysis demonstrated high thermal stability for the compound, compared to similar organic compounds. The structural, thermal stability, the presence of the polar nitro groups, and electronic properties of the compound allow it to be a promising candidate for DSSC applications.

Authors' contributions

IB lead the project, designed the experiments, analyzed data, and performed the theoretical calculations. IW performed the experimental work and analyzed results. ST, SR, and AZ participated in synthesizing the title compound. All authors read and approved the final manuscript.

Declaration of Competing Interest

The authors declare that they have no competing interests.

Acknowledgments

The authors are grateful to the College of Arts and Sciences at Qatar University, Hassan II University, Mohammed first University, and Mohammed V University for supporting this research. Open Access funding provided by the Qatar National Library.

Supplementary materials

Supplementary material associated with this article can be found, in the online version, at doi:10.1016/j.molstruc.2020.129799.

References

[1] A.G. Al-Sehemi, A. Irfan, A.M. Asiri, Y.A. Ammar, Synthesis, characterization and DFT study of methoxybenzylidene containing chromophores for DSSC materials, Spec. Acta Part A: Molecular and Biomolecular Spectroscopy 91 (2012) 239–243.
[2] H. Sun, J. Deng, L. Qiu, X. Fang, H. Peng, Recent progress in solar cells based on one-dimensional nanomaterials, Environ. Sci. 8 (4) (2015) 1139–1159.
[3] F. Labat, T.Le Bahers, I. Ciofini, C. Adamo, First-Principles Modeling of Dye-Sensitized Solar Cells: Challenges and Perspectives, Acc. Chem. Res. 45 (8) (2012) 1268–1277.
[4] J. Gong, K. Sumathy, Q. Qiao, Z. Zhou, Review on dye-sensitized solar cells (DSSCs): Advanced techniques and research trends, Renewable Sustainable Energy Rev 68 (2017) 234–246.
[5] Y. Jung, I.G. Ju, Y.H. Choe, Y. Kim, S. Park, Y.-M. Hyun, M.S. Oh, D. Kim, Hydrazine Exposé, The Next-Generation Fluorescent Probe, ACS Sensors 4 (2) (2019) 441–449.
[6] M.El Azzouzi, A. Aouniti, S. Tighadouin, H. Elmsellem, S. Radi, B. Hammouti, A.El Assyry, F. Bentiss, A. Zarrouk, Some hydrazine derivatives as corrosion inhibitors for mild steel in 1.0M HCl: Weight loss, electrochemichal, SEM and theoretical studies, J. Mol. Liq. 221 (2016) 633–641.
[7] M.E. Belghiti, S. Echihi, A. Dafali, Y. Karzazi, M. Bakasse, H. Elalaoui-Elabdallaoui, L.O. Olasunkanmi, E.E. Ebenso, M. Tabyaoui, Computational simulation and statistical analysis on the relationship between corrosion inhibition efficiency and molecular structure of some hydrazine derivatives in phosphoric acid on mild steel surface, Appl. Surf. Sci. 491 (2019) 707–722.
[8] P. Zhang, H. Wang, H. Liu, M. Li, Fluorescence-Enhanced Organogels and Mesomorphic Superstructure Based on Hydrazine Derivatives, Langmuir 26 (12) (2010) 10183–10190.
[9] J. Easmon, G. Pürstinger, K.-S. Thies, G. Heinisch, J. Hofmann, Synthesis, Structure−Activity Relationships, and Antitumor Studies of 2-Benzoxazolyl Hydrazones Derived from Alpha-(N)-acyl Heteroaromatics, J. Med. Chem. 49 (21) (2006) 6343–6350.
[10] N.V. Markova, M.I. Rogojerov, V.T. Angelova, N.G. Vassilev, Experimental and theoretical conformational studies of hydrazine derivatives bearing a chromene scaffold, J. Mol. Struct. 1198 (2019) 126880.
[11] K. Sharma, V. Sharma, S. Sharma, Dye-sensitized solar cells: fundamentals and current status, Nanoscale Res. Lett. 13 (1) (2018) 381.
[12] G. Boschloo, Improving the performance of dye-sensitized solar cells, Frontiers in chemistry 7 (2019).

[13] P. Ren, Y. Zhang, Z. Luo, P. Song, Y. Li, Theoretical and experimental study on spectra, electronic structure and photoelectric properties of three nature dyes used for solar cells, J. Mol. Liq. 247 (2017) 193–206.
[14] Y.-F. Chan, C.-C. Wang, C.-Y. Chen, Quasi-solid DSSC based on a gel-state electrolyte of PAN with 2-D graphenes incorporated, J. Mater. Chem. A 1 (18) (2013) 5479–5486.
[15] M. Suzuka, N. Hayashi, T. Sekiguchi, K. Sumioka, M. Takata, N. Hayo, H. Ikeda, K. Oyaizu, H. Nishide, A Quasi-Solid State DSSC with 10.1% Efficiency through Molecular Design of the Charge-Separation and -Transport, Sci. Rep. 6 (1) (2016) 28022.
[16] S. Shalini, R. Balasundaraprabhu, T.S. Kumar, N. Prabavathy, S. Senthilarasu, S. Prasanna, Status and outlook of sensitizers/dyes used in dye sensitized solar cells (DSSC): a review, Int. J. Energy Res. 40 (10) (2016) 1303–1320.
[17] S. Tighadouini, S. Radi, L. Toupet, M. Sirajuddin, T.B. Hadda, M. Akkurt, I. Warad, Y.N. Mabkhot, S. Ali, Origin and switch of different colors: Thermo-isomerism and crystal structure of (1E,2E)-bis[1-(4-nitrophenyl)ethylidene] hydrazine, J. Chem. Sci. 127 (12) (2015) 2211–2216.
[18] C.R. Groom, I.J. Bruno, M.P. Lightfoot, S.C. Ward, The Cambridge Structural Database, Acta Crystallographica Section B 72 (2) (2016) 171–179.
[19] B. Chen, X. Sun, X. Li, H. Ågren, Y. Xie, TICT based fluorescence "turn-on" hydrazine probes, Sens. Actuators, B 199 (2014) 93–100.
[20] S. Sasaki, G.P.C. Drummen, G.-i. Konishi, Recent advances in twisted intramolecular charge transfer (TICT) fluorescence and related phenomena in materials chemistry, J. Mater. Chem. C 4 (14) (2016) 2731–2743.
[21] N. Mardirossian, M. Head-Gordon, Thirty years of density functional theory in computational chemistry: an overview and extensive assessment of 200 density functionals, Mol. Phys. 115 (19) (2017) 2315–2372.
[22] H. Kruse, L. Goerigk, S. Grimme, Why the Standard B3LYP/6-31G* Model Chemistry Should Not Be Used in DFT Calculations of Molecular Thermochemistry: Understanding and Correcting the Problem, J. Org. Chem. 77 (23) (2012) 10824–10834.
[23] R. Peverati, D.G. Truhlar, Quest for a universal density functional: the accuracy of density functionals across a broad spectrum of databases in chemistry and physics, Philos. Trans. R. Soc. London, Ser. A 372 (2011) 20120476 (2014).
[24] M. Head-Gordon, J.A. Pople, M.J. Frisch, MP2 energy evaluation by direct methods, Chem. Phys. Lett. 153 (6) (1988) 503–506.
[25] J.S. Binkley, J.A. Pople, Møller–Plesset theory for atomic ground state energies, Int. J. Quantum Chem 9 (2) (1975) 229–236.
[26] S. Wolff, D. Grimwood, J. McKinnon, M. Turner, D. Jayatilaka, M. Spackman, CrystalExplorer (Version 3.1), University of Western Australia, 2012.
[27] C.F. Macrae, I. Sovago, S.J. Cottrell, P.T. Galek, P. McCabe, E. Pidcock, M. Platings, G.P. Shields, J.S. Stevens, M. Towler, Mercury 4.0: from visualization to analysis, design and prediction, J. Appl. Crystallogr. (2020).
[28] A.D. Becke, Density-functional thermochemistry. III. The role of exact exchange, J. Chem. Phys. 98 (7) (1993) 5648–5652.
[29] A.D. Becke, A new mixing of Hartree–Fock and local density-functional theories, J. Chem. Phys. 98 (2) (1993) 1372–1377.
[30] J.P. Perdew, Y. Wang, Accurate and simple analytic representation of the electron-gas correlation energy, Phys. Rev. B: Condens. Matter 45 (23) (1992) 13244.
[31] J. Tao, J.P. Perdew, V.N. Staroverov, G.E. Scuseria, Climbing the density functional ladder: Nonempirical meta–generalized gradient approximation designed for molecules and solids, Phys. Rev. Lett. 91 (14) (2003) 146401.
[32] A. Austin, G.A. Petersson, M.J. Frisch, F.J. Dobek, G. Scalmani, K. Throssell, A Density Functional with Spherical Atom Dispersion Terms, J. Chem. Theory Comput. 8 (12) (2012) 4989–5007.
[33] S.Y. Haoyu, X. He, S.L. Li, D.G. Truhlar, MN15: A Kohn–Sham global-hybrid exchange–correlation density functional with broad accuracy for multi-reference and single-reference systems and noncovalent interactions, Chemical science 7 (8) (2016) 5032–5051.
[34] R. Peverati, D.G. Truhlar, Screened-exchange density functionals with broad accuracy for chemistry and solid-state physics, Phys. Chem. Chem. Phys. 14 (47) (2012) 16187–16191.
[35] I. Badran, Hot-wire chemical vapour deposition chemistry and kinetics of new precursors in the gas phase and on the wire surface, Department of Chemistry, University of Calgary, Calgary, Alberta, Canada, 2014.
[36] I. Badran, A. Hassan, A.D. Manasrah, N.N. Nassar, Experimental and theoretical studies on the thermal decomposition of metformin, J. Therm. Anal. Calorim. 138 (1) (2019) 433–441.
[37] I. Badran, A. Rauk, Y.J. Shi, Theoretical Study on the Ring-Opening of 1,3-Disilacyclobutane and H2 Elimination, J. Phys. Chem. A 116 (48) (2012) 11806–11816.
[38] I. Warad, S. Musameh, I. Badran, N.N. Nassar, P. Brandao, C.J. Tavares, A. Barakat, Synthesis, solvatochromism and crystal structure of trans-[Cu(Et2NCH2CH2NH2)2.H2O](NO3)2 complex: Experimental with DFT combination, J. Mol. Struct. 1148 (2017) 328–338.
[39] I. Badran, L. Abdallah, R. Mubarakeh, I. Warad, Effect of alkyl derivation on the chemical and antibacterial properties of newly synthesized Cu (II)-diamine complexes, Moroccan Journal of Chemistry 7 (1) (2019) 161–170 7-1 (2019).
[40] M. Cossi, G. Scalmani, N. Rega, V. Barone, New developments in the polarizable continuum model for quantum mechanical and classical calculations on molecules in solution, J. Chem. Phys. 117 (1) (2002) 43–54.
[41] M. Cossi, V. Barone, R. Cammi, J. Tomasi, Ab initio study of solvated molecules: a new implementation of the polarizable continuum model, Chem. Phys. Lett. 255 (4) (1996) 327–335.
[42] I. Badran, N.N. Nassar, N.N. Marei, A. Hassan, Theoretical and thermogravimetric study on the thermo-oxidative decomposition of Quinolin-65 as an asphaltene model molecule, RSC Advances 6 (59) (2016) 54418–54430.
[43] I. Badran, A. Rauk, Y. Shi, New Orbital Symmetry-Allowed Route for Cycloreversion of Silacyclobutane and Its Methyl Derivatives, J. Phys. Chem. A 123 (9) (2019) 1749–1757.
[44] M.J. Frisch, G.W. Trucks, H.B. Schlegel, G.E. Scuseria, M.A. Robb, J.R. Cheeseman, G. Scalmani, V. Barone, G.A. Petersson, H. Nakatsuji, X. Li, M. Caricato, A.V. Marenich, J. Bloino, B.G. Janesko, R. Gomperts, B. Mennucci, H.P. Hratchian, J.V. Ortiz, A.F. Izmaylov, J.L. Sonnenberg, Williams, F. Ding, F. Lipparini, F. Egidi, J. Goings, B. Peng, A. Petrone, T. Henderson, D. Ranasinghe, V.G. Zakrzewski, J. Gao, N. Rega, G. Zheng, W. Liang, M. Hada, M. Ehara, K. Toyota, R. Fukuda, J. Hasegawa, M. Ishida, T. Nakajima, Y. Honda, O. Kitao, H. Nakai, T. Vreven, K. Throssell, J.A. Montgomery Jr., J.E. Peralta, F. Ogliaro, M.J. Bearpark, J.J. Heyd, E.N. Brothers, K.N. Kudin, V.N. Staroverov, T.A. Keith, R. Kobayashi, J. Normand, K. Raghavachari, A.P. Rendell, J.C. Burant, S.S. Iyengar, J. Tomasi, M. Cossi, J.M. Millam, M. Klene, C. Adamo, R. Cammi, J.W. Ochterski, R.L. Martin, K. Morokuma, O. Farkas, J.B. Foresman, D.J. Fox, Gaussian 16 Rev. C.01, Wallingford, CT, 2016.
[45] R. Dennington, T. Keith, J. Millam, GaussView, version 5, (2009).
[46] D. Braga, F. Grepioni, G.R. Desiraju, Crystal engineering and organometallic architecture, Chem. Rev. 98 (4) (1998) 1375–1406.
[47] G.R. Desiraju, Supramolecular Synthons in Crystal Engineering—A New Organic Synthesis, Angew. Chem. Int. Ed. 34 (21) (1995) 2311–2327.
[48] N. Al-Zaqri, K.S.M. Salih, F.F. Awwadi, A. Alsalme, F.A. Alharthi, A. Alsyahi, A.A. Ali, A. Zarrouk, M. Aljohani, A. Chetouni, I. Warad, Synthesis, physicochemical, thermal, and XRD/HSA interactions of mixed [Cu(Bipy)(Dipn)](X)2 complexes: DNA binding and molecular docking evaluation, J. Coord. Chem. (2020) 1–13.
[49] F.A. Saleemh, S. Musameh, A. Sawafta, P. Brandao, C.J. Tavares, S. Ferdov, A. Barakat, A.A. Ali, M. Al-Noaimi, I. Warad, Diethylenetriamine/diamines/copper (II) complexes [Cu(dien)(NN)]Br2: Synthesis, solvatochromism, thermal, electrochemistry, single crystal, Hirshfeld surface analysis and antibacterial activity, Arab. J. Chem. 10 (6) (2017) 845–854.
[50] I. Warad, S. Musameh, A. Sawafta, P. Brandão, C. José Tavares, A. Zarrouk, S. Amereih, A. Al Ali, R. Shariah, Ultrasonic synthesis of Oct. trans-Br2Cu(N ∩ N)2 Jahn-Teller distortion complex: XRD-properties, solvatochromism, thermal, kinetic and DNA-binding evaluations, Ultrason. Sonochem. 52 (2019) 428–436.
[51] D.D. Babu, P. Naik, K.S. Keremane, A simple D-A-π-A configured carbazole based dye as an active photo-sensitizer: A comparative investigation on different parameters of cell, J. Mol. Liq. 310 (2020) 113189.
[52] J. Tauc, A. Menth, States in the gap, J. Non-Cryst. Solids 8 (1972) 569–585.
[53] J.R. Lakowicz, Principles of fluorescence spectroscopy, Springer Science & Business Media, 233 Spring Street, New York, NY 10013, USA, 2013.
[54] C. Gell, D. Brockwell, A. Smith, Handbook of single molecule fluorescence spectroscopy, Oxford University Press Great Clarendon Street, Oxford, OX2 6DP, UK, 2006.
[55] A. Guerraoui, A. Djedouani, E. Jeanneau, A. Boumaza, A. Alsalme, A. Zarrouk, K.S.M. Salih, I. Warad, Crystal structure and spectral of new hydrazine-pyran–dione derivative: DFT enol↔hydrazone tautomerization via zwitterionic intermediate, hirshfeld analysis and optical activity studies, J. Mol. Struct. 1220 (2020) 128728.
[56] M. Ikram, S. Rehman, R.J. Baker, H.U. Rehman, A. Khan, M.I. Choudhary, Synthesis and distinct urease enzyme inhibitory activities of metal complexes of Schiff-base ligands: Kinetic and thermodynamic parameters evaluation from TG-DTA analysis, Thermochim. Acta 555 (2013) 72–80.
[57] I. Badran, A.D. Manasrah, A. Hassan, N.N. Nassar, Kinetic study of the thermo-oxidative decomposition of metformin by isoconversional and theoretical methods, Thermochim. Acta (2020) 178797.